Development of Micromechanics Models and Innovative Sensor Technologies to Evaluate Internal Frost Damage of Concrete

Qingli Dai, Xiong Yu, Kenny Ng, and Zhen Liu

Internal frost damage is a major problem affecting the durability of concrete in cold regions. Micromechanics models and innovative sensor technologies were used to study the mechanisms of frost damage in concrete. Crystallization pressure resulting from ice nucleation within capillary pores is the primary cause of internal frost damage of concrete. Crystallization pressure of a cylinder pore was formulated with interface energy balance with thermodynamics analysis. Crystallization pressure on the pore wall was input for fracture simulation with the extended finite element model on a homogeneous beam sample with a vertical cylinder pore; this simulation led to a straight line. An image sample was obtained with imaging process and ellipse fitting techniques to capture microstructure of a tested specimen. Crack simulation of this image sample with the same cylinder pore under crystallization pressure matched fracture patterns of the single-edge-notched bending specimen. Extended finite element model simulation results were verified by open-mode fracture behavior in middle-notched single-edge-notched bending and freezing tests. An innovative time-domain reflectometry sensor was developed to nondestructively monitor the freezing process. Data show that sensor signals from time-domain reflectometry can detect the freezing degree, an important input parameter. Studies indicate that the micromechanics models and time-domain reflectometry sensor techniques can help practitioners evaluate internal frost damage of concrete. Future work will incorporate sensor measurements into micromechanics models to predict, in real time, internal frost damage process in concrete specimens. The goal of this study was to provide practical nondestructive testing and computational tools for designing concrete that is resistant to freezing damage.

Concrete is one of the most widely used construction materials in the world. According to published information from the Portland Cement Association, more than 320 million yards of concrete are placed each year in America (*1*). With concrete an essential component of the U.S. infrastructure system, its durability has significant impacts on maintenance costs. In cold climates, freeze-thaw damage is a major problem reducing the durability of concrete. Consequences are increased repair and replacement expenditures. Deleterious effects of the freeze–thaw cycle depend on the microscale characteristics of concrete, such as pore size and pore distribution, as well as environmental conditions.

The frost-induced damage of concrete under freeze–thaw cycles has different forms (Figure 1). A common type is cracking and spalling of non-air-entrained or poorly air-entrained concrete caused by the progressive expansion of the cement paste matrix from repeated freezing and thawing cycles (Figure 1*a*). A D-shaped cracking pattern (Figure 1*b*) in the slab of concrete pavement is generally associated with coarse aggregates, which contain a proportionately greater pore volume (pore size ranging from 0.1 to 1 μm) (*4*).

According to the theory advanced by Litvan, the tightly held water by the calcium-silicate-hydrate (C-S-H) in cement paste cannot rearrange itself to form ice at the normal freezing point of water because the mobility of water constrained in an ordered state is rather limited (*5*). Generally, the more tightly water is held, the lower is the freezing point. The relationship between pore sizes and freezing–melting temperature is formulated based on thermodynamics (*6*).

Limiting the average air void spacing to 250 to 300 μm can prevent the deleterious expansion of cement paste upon internal crystallization (*7*). Figure 2*a* indicates the dilation of non-air-entrained samples and contraction of an air-entrained sample when the temperature drops. The adequately air-entrained paste contracts on freezing because ice crystals within air voids draw water from the surrounding porous matrix.

Recent theories attribute the damage from freezing of concrete to be the result of crystallization pressure (*8–10*). The stress exerted on porous bodies by crystals of ice follows from the fact that the solids repel with one another. A film of liquid (thickness δ) separates the surfaces of the growing crystal and the pore wall. The van der Waals forces of ice alone provide a large enough repulsive force to exceed the tensile strength of concrete and push ice into contact with mineral surfaces. To avoid destructive pressure from the growth of ice in the pores, larger air voids are provided as nucleation sites for ice. They also accommodate the expansion of volume caused by crystallization. As will be explained, crystals in the voids draw in liquid from the small pores

Q. Dai and K. Ng, Department of Civil and Environmental Engineering, Michigan Technological University, 1400 Townsend Drive, Houghton, MI 49931-1295. X. Yu, Bingham 210, and Z. Liu, Bingham 257, Department of Civil Engineering, Case School of Engineering, Case Western Reserve University, 10900 Euclid Avenue, Cleveland, OH 44106-7201. Corresponding author: Q. Dai, qingdai@mtu.edu.

Transportation Research Record: Journal of the Transportation Research Board, No. 2240, Transportation Research Board of the National Academies, Washington, D.C., 2011, pp. 50–58.
DOI: 10.3141/2240-08

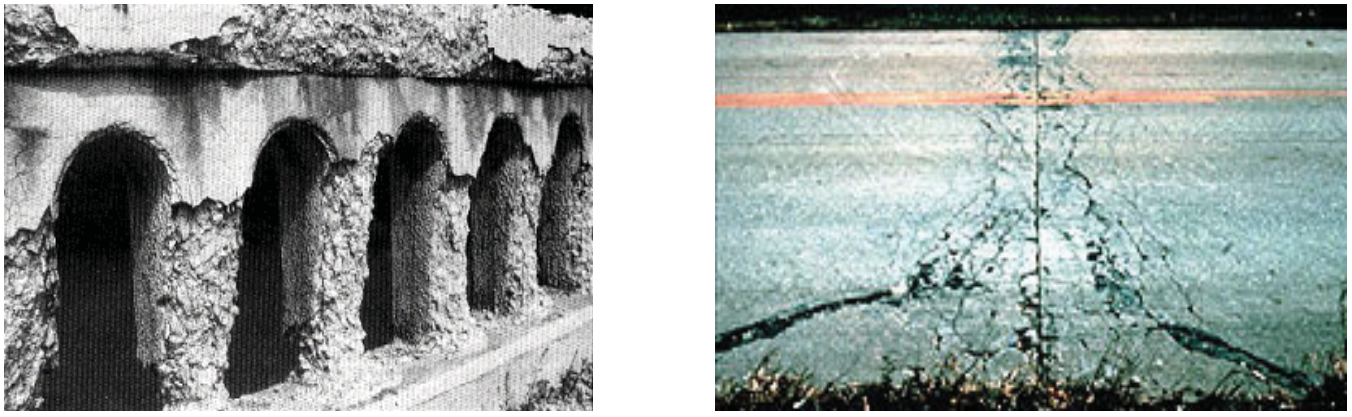

(a) (b)

FIGURE 1 Types of freeze–thaw damage in concrete: (*a*) deterioration of non-air-entrained concrete (*3*) and (*b*) severe D-cracking damage in slab concrete pavement (*2*).

of paste (pore radius $r_P < 50$ nm) and thereby impose compressive stresses on the concrete. The relationship between melting point (T_m) and pore size (radius, r_P) is given by the Gibbs-Thomson equation (*11*):

$$T_m(\kappa_{CL}) = T_m(0) - \frac{\gamma_{CL}\kappa_{CL}}{\Delta S_{FV}} \quad (1)$$

where

$T_m(\kappa_{CL})$ = threshold temperature for forming crystals in capillary pores,
γ_{CL} = crystal–liquid interfacial energy,
κ_{CL} = curvature of the crystal–liquid interface related to pore radius r_P, and
ΔS_{FV} = entropy of fusion per unit volume of crystal.

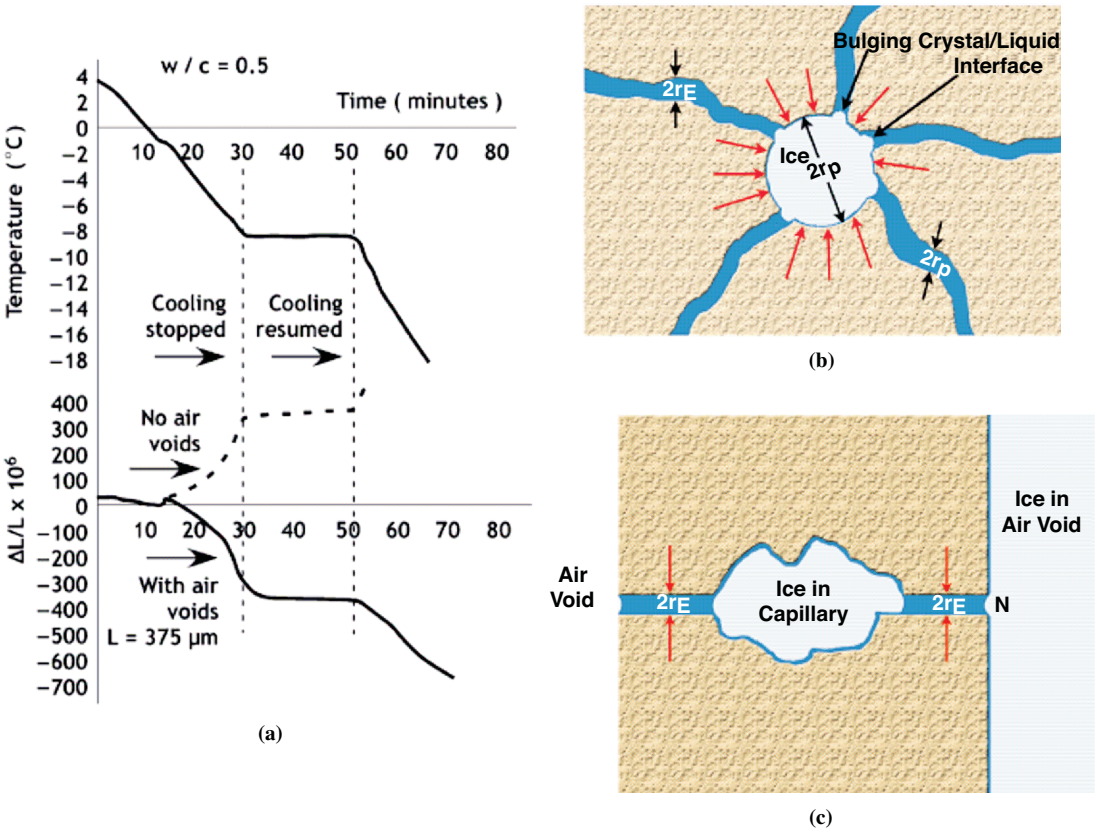

(a) (b) (c)

FIGURE 2 Graphs and schematics: (*a*) reversed volume change by reduction of average air void spacing—dilation of a non-air-entrained sample and contraction of an air-entrained sample (*7*); (*b*) ice confined in a capillary pore ($r_p < 50$ nm), but unable to penetrate into intersecting pores (*8*); and (*c*) ice forming in a capillary void and in an air void (*8*).

Under temperature $T < T_m(\kappa_{CL})$, the crystal will bulge into the mouths of intersecting pores (the intersection pore radius $r_E < r_P$) until the curvature satisfies Equation 1 (Figure 2*b*). To be in equilibrium, the pore wall imposes a confining pressure on the surface of the crystal (indicated with red arrows in Figure 2*b* and 2*c*), and this results in tensile stress in the pore wall. The confining pressure and tensile stress is proportional to the difference of the curvature of the confining pore and crystal surface. This tensile stress will initiate microcracking and weaken the concrete during internal freezing (*8*).

The ice can exist in the capillary pores and in the larger air voids simultaneously under a subcooling condition (shown in Figure 2*c*). That is because the formed ice can draw fluid from the capillary pores. The ice penetration is accompanied with the suction of the pore solution surrounding the void, compressing the porous concrete. As the temperature is further reduced, ice is able to access more of the pore space. The damaging stresses are induced under two possible situations: ice escapes from a large void by passing a constriction and ice grows into a zone of saturated microstructure encapsulated by the invading ice (*10*).

OBJECTIVE AND SCOPE

The objective of this study is to develop micromechanics models and innovative sensor techniques to evaluate the internal frost damage of concrete, one of the most important factors affecting the durability of concrete infrastructure in cold regions. In addition, this study aims to provide a practical tool by combining micromechanics model and sensor technology to facilitate optimized design for avoiding the excessive frost damage of concrete. In this paper, three correlated work will be presented to study the internal frost damage of heterogeneous concrete:

1. Crystallization pressure because of ice nucleation in concrete pore system is formulated with thermodynamics analysis.
2. Crystallization pressure is obtained from a vertical cylinder pore with hemispherical end in the middle of concrete beam samples. The developed extended finite element model (XFEM) is used to simulate the crack propagation of a homogeneous beam sample and an imaging beam sample under crystallization pressure. The predicted crack propagation of the imaging sample is compared with the tested middle-notched bending beam specimen because of open-mode crack propagation in both loading cases.
3. An innovative time-domain reflectometry (TDR) tube sensor is developed to nondestructively monitor the freezing process. The TDR tube sensor signals are used for determining the freezing status of concrete specimen.

The developed TDR tube sensor can detect the amount of formed ice from the saturated water within pore system in real time. This information helps to calculate the crystallization pressure generated from specific pores. With these calculated pressures, the developed micromechanics model can simultaneously predict the crack propagation under freezing process.

CRYSTALLIZATION PRESSURE WITHIN A SATURATED PORE

The magnitude of stress applied by ice crystals in the capillary pores has been investigated by several researchers using thermodynamics analysis (*11–13*). The basic thermodynamic equation for the energy balance at the interfaces of three phases of water (i.e., vapor, liquid and solid) in the pores is given as follows (*11*):

$$v_c\left(P_A + \gamma_{CL}\kappa_{CL}\right) = \left(v_L - v_c\right)\left(P_L - P_e\right) + \left(S_L - S_C\right)\left(T_m - T\right) \tag{2}$$

where

v_c = molar volume of crystal,
P_A = applied pressure to liquid,
v_L = molar volume of water,
P_L = liquid pressure,
P_e = equilibrium vapor pressure,
S_L = entropy of pure water, and
S_C = entropy of crystal ice.

Recall that γ_{CL} is crystal–liquid interfacial energy, κ_{CL} is curvature of crystal–liquid interface, T_m is melting temperature, and T is a subcooling temperature. If the liquid–vapor menisci are flat ($P_L = P_e$) and $P_A = 0$, Equation 2 will reduce to the Gibbs-Thomson equation (*11*).

Laplace's equation relates the pressure in the liquid to the curvature of the liquid–vapor interface as $P_L - P_e = \gamma_{LV}\kappa_{LV}$, where γ_{LV} is the liquid–vapor interfacial energy, and κ_{LV} is the curvature of the liquid-vapor interface (*14*). Thus, Equation 2 can be written as follows (*11*):

$$v_c\left(P_A + \gamma_{CL}\kappa_{CL}\right) = \left(v_L - v_c\right)\gamma_{LV}\kappa_{LV} + \left(S_L - S_C\right)\left(T_m - T\right) \tag{3}$$

As mentioned earlier, the internal frost cracks will grow when the crystals propagate through the pore space. The greatest crystallization pressure occurs when a film of liquid (thickness δ) is present at the interface between the crystal and pore wall (*12*).

For example, crystallization pressure is generated in two connected pores with small entries at a subcooling temperature *T,* as shown in Figure 3. At point *P,* with relative flat curve (small curvature), the pore wall imposes the highest pressure on the ice crystal, whereas at point *N,* with negative curvature, the pore wall protrudes into the crystal. Assume the relative humidity and temperature is the same for this ice crystal; the right side of Equation 3 is in balance with the entry end where $P_A = 0$ and the curvature is κ_{CL}^{E}. Thus the crystallization pressure changes with curvature at different internal points (*11*):

$$P_A = \gamma_{CL}\left(\kappa_{CL}^{E} - \kappa_{CL}^{S}\right) \tag{4}$$

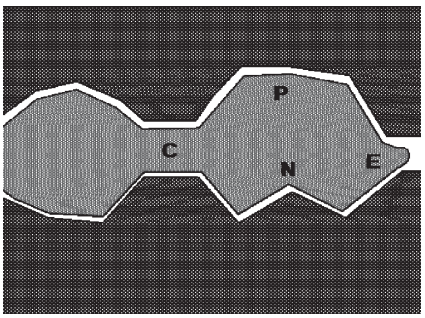

FIGURE 3 Illustration of crystal of ice in two connected pores: E = pore entry, C = constriction, P = large positive curvature, and N = small negative curvature.

At the constriction C, the channel curvature κ_{CL}^{S} is very small and the pressure $P_A \approx \gamma_{CL}\kappa_{CL}^{E}$.

MICROMECHANICS MODELS TO PREDICT FROST DAMAGE UNDER CRYSTALLIZATION PRESSURE

Extended Finite Element Model

The XFEM was developed to predict the crack propagation within heterogeneous concrete, and this approach allows crack grow within elements and thus eliminates remeshing efforts. This section briefly presents the XFEM formulation for simulating the two-dimensional crack and inclusion problems. Enrichment functions and level set functions for cracks and inclusions used in the XFEM will be explained. The calculation of fracture properties including *J*-integral and stress intensity factors K_I and K_{II} and the determination of crack propagation will also be briefly described.

Crack Enrichment

For the crack problem, the Heaviside and crack tip enrichments were defined in the crack domain $\Omega = \Omega^1 + \Omega^2$, as shown in Figure 4*a*. The enriched displacement function $u^h(x)$ in XFEM is given in the form that follows (*15*):

$$u^h(x) = \sum_{i\in I} u_i N_i + \sum_{j\in J} b_j N_j H(x) + \sum_{k\in K} N_k \left(\sum_{l=1}^{4} c_k^l F_l(x) \right) \tag{5}$$

where

u_i = traditional finite element degrees of freedom;
N_i = traditional finite element shape functions of node i;
b_j = additional degrees of freedom associated with Heaviside function enrichment functions (circled nodes as shown in Figure 4*a*);
N_j = shape function associated with the Heaviside function at node j;
$H(x)$ = Heaviside or jump function;
N_k = shape function associated with enriched crack tip function at node k;
c_k^l = additional degrees of freedom associated with elastic asymptotic crack-tip enrichment functions (square nodes as shown in Figure 4*a*);
$F_l(x)$ = crack-tip enrichment function, where l is the term index;
I = set of all nodes in the mesh;
J = set of Heaviside enriched nodes whose shape functions are cut by the crack path; and
K = set of crack-tip-enriched nodes whose shape functions are cut by the crack tip.

A visual representation of the enriched nodes in a crack domain is shown in Figure 4*a*. For the nonenriched domains, the displacement functions reduced to the traditional finite element method:

$$u^h(x) = \sum_{i\in I} u_i N_i \tag{6}$$

In the crack domain Ω^1, which has only the crack surface without the crack tip, the displacement functions can be written with Heaviside enrichments function, as follows:

$$u^h(x) = \sum_{i\in I} u_i N_i + \sum_{j\in J} b_j N_j H(x) \tag{7}$$

For the crack domain Ω^2, which consists of crack tip, the displacement functions can be formulated with the crack-tip enrichments function as follows:

$$u^h(x) = \sum_{i\in I} u_i N_i + \sum_{k\in K} N_k \left(\sum_{l=1}^{4} c_k^l F_l(x) \right) \tag{8}$$

In the XFEM, the level set method is applied to track the crack surface and crack-tip geometry while the crack is growing in each step (*16*). For the two-dimensional analysis, the Heaviside function $H(x)$ is defined with a crack-surface level-set function $\phi(x)$, which describes the discontinuity across the crack surfaces within an element and takes the following form:

$$H(x) = \text{sign}(\phi(x)) = \begin{cases} -1 & \phi(x) < 0 \\ 0 & \phi(x) = 0 \\ +1 & \phi(x) > 0 \end{cases} \tag{9}$$

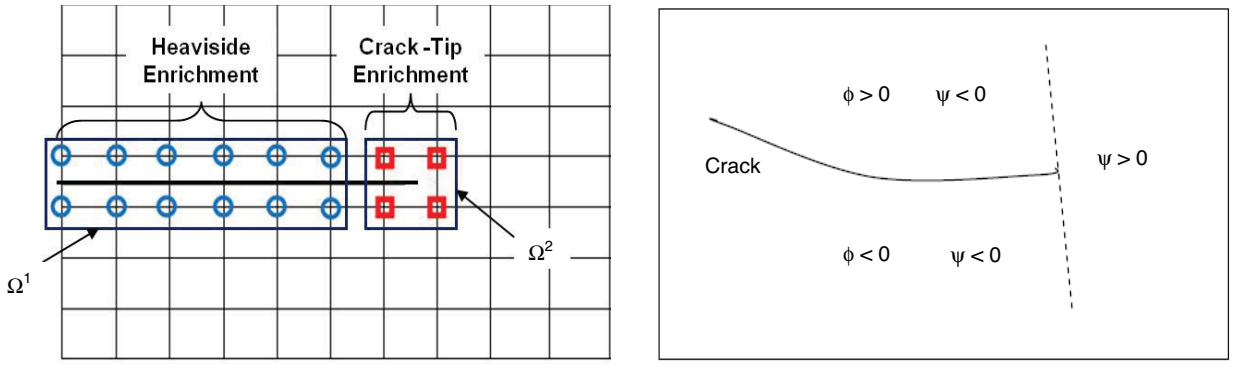

FIGURE 4 Crack enrichment and crack geometry in XFEM: (*a*) schematic of Heaviside and crack-tip enrichments defined on nodes in crack domain and (*b*) level set methods that represent geometry of crack surface and crack front boundary.

where $\phi(x)$ is the crack-surface level set function that represents the signed distance from a node to the crack surface and the tangent extension from the crack front. The crack-tip level set function $\psi(x)$ is the signed distance function that describes the position of the crack tip with respect to the node in the normal direction, as shown in Figure 4*b*.

The crack-tip enrichment function, which defines the discontinuity at the crack tip within an element, takes the form of four functions as follows:

$$\left[F_l(r,\theta), l=1-4\right]=\left[\begin{array}{l}\sqrt{r}\sin\dfrac{\theta}{2},\sqrt{r}\cos\dfrac{\theta}{2},\\ \sqrt{r}\sin\theta\sin\dfrac{\theta}{2},\sqrt{r}\sin\theta\cos\dfrac{\theta}{2}\end{array}\right] \tag{10}$$

where r and θ are the polar coordinates in the local crack-tip coordinate system.

Inclusion Enrichment

Along the inclusion interface, the enriched displacement function $u^h(x)$ can be written as follows:

$$u^h(x)=\sum_{i\in I}u_iN_i+\sum_{m\in M}N_m a_m F(x) \tag{11}$$

where m is the degrees of freedom index, and M is the total number of degrees of freedom in an inclusion-enriched element. The additional degrees of freedom a_m were defined at the nodes where the elements are divided by the inclusion interface. The enrichment function $F(x)$ was taken as the following form to describe the discontinuity such as debonding behavior in the aggregate–cement interfacial transition zones with improved convergence (*17, 18*):

$$F(x)=\sum_{k\in K}N_k(x)|\zeta_k|-\left|\sum_k N_k(x)\zeta_k\right| \tag{12}$$

where K is the number of inclusions and $\zeta_k(x)$ is the level set function for each inclusion. For the ellipse inclusion, $\zeta_k(x)$ is defined as follows:

$$\zeta_k(x)=\frac{\left[(x_i-x_c)\cos\theta+(y_i-y_c)\sin\theta\right]^2}{a^2}+\frac{\left[(y_i-y_c)\cos\theta+(x_i-x_c)\sin\theta\right]^2}{b^2}-1 \tag{13}$$

where

x_i and y_i = coordinates of the ith node in the domain,
x_c and y_c = center coordinates of the elliptical inclusion, and
a and b = lengths of the major and minor axes of the ellipse, respectively.

Crack Growth and Stress Intensity Factors

In the XFEM, the J-integral (J_1) and the stress intensity factors are used to determine the crack growth. For the crack-tip opening along the global x-direction, the J-integral equation is given in the following form:

$$J_1=\int_\Gamma\left[W\delta_{1j}-\sigma_{ij}\frac{\partial u_i}{\partial x_1}\right]\eta_j d\Gamma \tag{14}$$

where

W = strain energy density,
1 = crack-tip opening along global x-direction,
σ = Cauchy stress tensor,
η = normal vector to integration curve Γ, and
u = displacement vector.

It has been proved that using the two-state J-integral approach can generate the stress intensity factor on a crack tip more efficiently (*19*). The stress intensity factors are determined the two-state J-integral approach. The Mode I stress intensity factor is given as follows:

$$K_I=\frac{1}{2}E_{\text{eff}}I^{(\text{Mode I})} \tag{15}$$

where E_{eff} is the effective modulus, and $I^{(\text{Mode I})}$ is the interaction term of two-state interaction term of the J-integral. Similarly, the Mode II stress intensity factor generates the following term:

$$K_{II}=\frac{1}{2}E_{\text{eff}}I^{(\text{Mode II})} \tag{16}$$

where $I^{(\text{Mode II})}$ is also the interaction integrals. After obtaining both stress intensity factors, the Paris crack growth law was used to determine the crack growth (*20*). The maximum circumferential stress criterion is applied for crack propagation in the direction with the maximum circumferential stress $\sigma_{\theta\theta}$. The angle of crack growth is obtained as follows:

$$\theta_c=2\arctan\frac{1}{4}\left(\frac{K_I}{K_{II}}-\text{sign}(K_{II})\sqrt{\left(\frac{K_I}{K_{II}}\right)^2+8}\right) \tag{17}$$

Crack Propagation on Beam Samples Under Crystallization Pressure

Homogeneous Beam Sample

The XFEM simulation was first conducted on a homogeneous beam sample, as shown in Figure 5. The beam sample was fixed on the bottom surface. A vertical cylinder pore with hemispherical end is located in the middle of the sample. The dimensions of this beam sample are about 50.8 μm wide, 50.8 μm thick, and 200.3 μm long. The radius (r_p) of the cylinder pore as shown in Figure 5*a* is about 34 nm. The sample was fully saturated and a layer of water was placed on the top surface, and the cylinder pore was filled with water. With the radius about 34 nm, the freezing temperature of the water inside of this cylinder pore can be calculated with Equation 1. For the ice, the crystal–liquid interfacial energy γ_{CL} is about 0.042 J/m^2 and entropy of fusion per unit volume of crystal ΔS_{FV} is about 1.2J/(cm^3-K) (*21*). The curvature of the crystal–liquid interface κ_{CL} is about $1/r_p$. The freezing temperature is reduced by 2.05°C

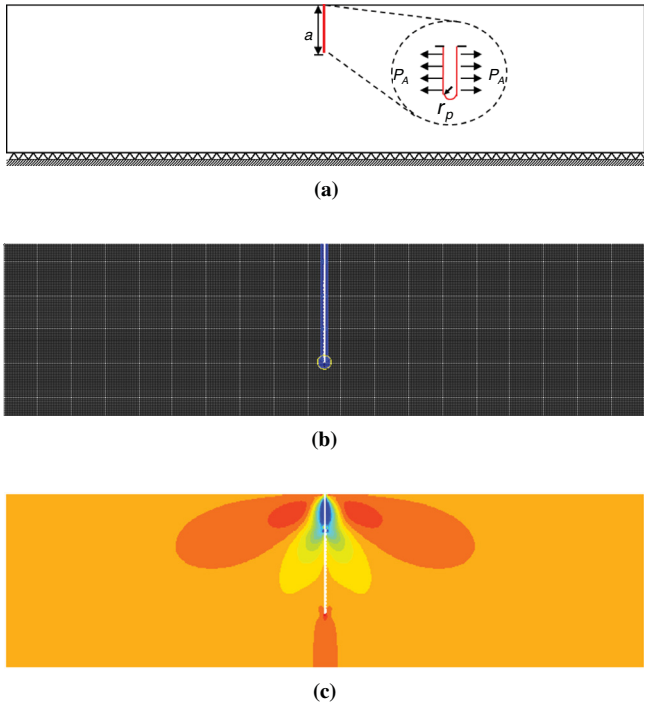

FIGURE 5 XFEM simulation of frost damage under crystallization pressure: (*a*) homogeneous middle-notched beam with distributed pressure *P* along notch surfaces and fixed support along the bottom surface, (*b*) mesh plot with propagated vertical crack, and (*c*) σ_{yy} contour plot from XFEM model.

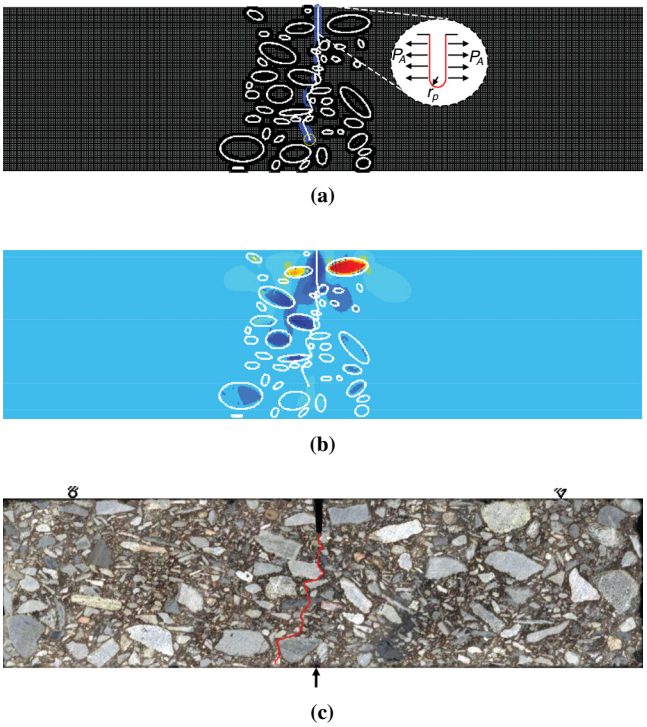

FIGURE 6 Frost damage simulation on an imaging beam sample using XFEM: (*a*) mesh plot with propagated crack caused by crystallization pressure, (*b*) σ_{yy} contour plot from XFEM model, and (*c*) fracture pattern of middle-notched bending beam specimen.

inside of this cylinder pore. Under a subcooling temperature below –2.05°C, the crystallization pressure with formed ice was generated at about 1.23 MPa, and the related loop stress exceeds the tensile stress of concrete. Thus, the crack started to propagate as a straight crack line under the uniform crystallization pressure onto a concrete wall (shown in Figure 5*b* and 5*c*).

Imaging Beam Sample

The XFEM fracture simulation was also conducted on an imaging beam sample, as shown in Figure 6. To model the laboratory specimens with idealized elliptical or circular geometry in the XFEM, the imaging analysis was performed. The microstructure of laboratory-tested specimens were captured through imaging processing with the available programs including the ImageJ, MATLAB image toolbox, and DIPimage toolbox for MATLAB. As shown in Figure 6, the aggregates in the middle section were identified and these aggregates were fitted with ellipses. The detailed imaging processing and aggregate ellipse fitting techniques can be found in previous work (*22*). Dimensions of this sample and the cylinder pore are same as for the homogeneous one. The generated crystallization pressure initiated the crack propagation within ellipse particle system. Because the sample under symmetric crystallization pressure generates open-mode crack propagation (Figure 6*a* and 6*b*), same as for the middle-notched beam bending test, the crack path was compared with the tested bending beam sample (Figure 6*c*), which was rotated 180° from the actual beam test position. The rotated test specimen has the top-down crack propagation as the simulated sample under crystallization pressure. The predicted crack propagation path of imaging sample matches well with the tested specimen, as shown in Figure 6. This also indicates that the developed XFEM approach can be used to simulate frost damage within a heterogeneous concrete microstructure.

TIME-DOMAIN REFLECTOMETRY SENSOR TO MONITOR FREEZING STATUS

Background on Time-Domain Reflectometry

TDR is an established technology for soil water content measurement [ASTM D6565, ASTM D6780 (*23, 24*)]. It features the advantages of being rugged, accurate, and automatic. This technology has been included in many field studies on pavement performance. A typical TDR system includes a TDR device (pulse generator and sampler), connection cable, and measurement probe (Figure 7). The measurement probe is surrounded by materials whose properties are to be measured. TDR works by sending a fast-rising step pulse or impulse to the measurement sensor and measuring the reflections resulting from the change of system geometry or material dielectric permittivity.

Figure 8 shows a typical measured TDR waveform. Dielectric constant (typically referred to as apparent dielectric constant and denoted as K_a in this paper) and electrical conductivity (denoted as EC_b in this paper) can be obtained from direct analysis of the TDR signal. The dielectric constant is related to the speed of electromagnetic wave in soils, and electrical conductivity is related to the rate of attenuation of electromagnetic wave. The dielectric constant by TDR is generally called apparent dielectric constant and is calculated by Equation 18.

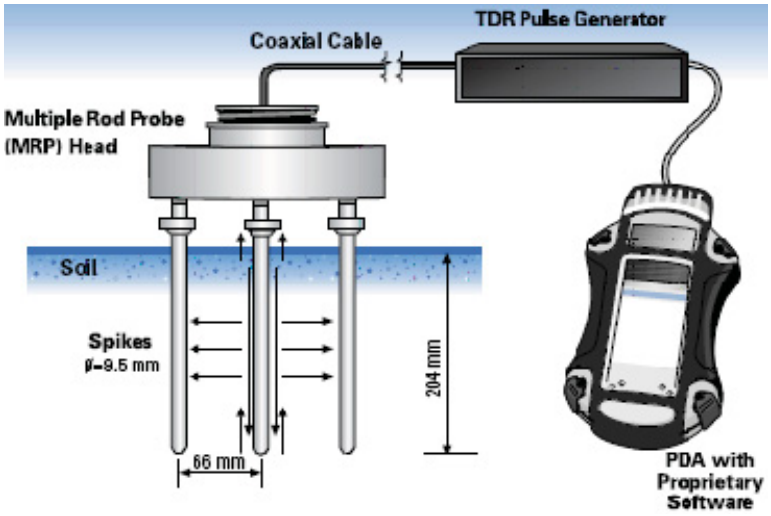

FIGURE 7 Schematic of TDR measurement system.

$$K_a = \left(\frac{L_a}{L_p}\right)^2 \tag{18}$$

where L_a is the apparent length obtained from the TDR waveform and L_p is the length of metallic probe embedded in soil.

The calculated apparent dielectric constant, K_a, in Equation 18 is a measurement of the bulk soil mixture. A granular mixture (such as soil or concrete) contains soil solids, water, and air. Because water has a much larger dielectric constant (around 81) than the other phases (around 3 to 7 for solids, depending on composition and texture, and 1 for air), the bulk dielectric constant strongly depends on the water content. A number of empirical equations relate the water content of soils to TDR measured apparent dielectric constant, including the classic Topp equation (*25*). Most of these equations use the concept of volumetric water content, whereas the concept of gravimetric water content is generally used for geotechnical applications. Equation 19, which was developed by Siddiqui and Drnevich, is unique in that it accounts for the effects of soil density and soil type (*26*):

$$w = \frac{1}{b}\left(\frac{\rho_w}{\rho_d}\sqrt{K_a} - a\right) \tag{19}$$

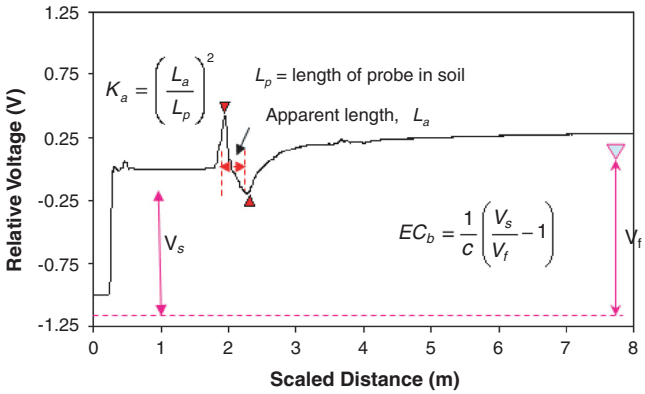

FIGURE 8 Example of measured TDR signal.

where

w = gravimetric water content,
ρ_w = density of water,
ρ_d = dry density of soil, and
a and b = materials-dependent calibration constants.

The application of TDR to frozen concrete is the natural extension of its application in measuring the soil water content. Compared with natural soil, the frozen concrete is a four-phase system containing solid mineral particles; ice inclusions (cementing ice and interlayer ice); water in the bound and liquid states; and air. Unfrozen water content is a real indicator, instead of temperature, of freezing and thawing status. The degree of freeze–thaw can thus be defined as the percentage change of liquid water content, that is,

$$\text{freeze}(\%) = \frac{w_{\text{unfrozen}} - w_t}{w_{\text{unfrozen}} - w_{\text{frozen}}} \times 100\% \tag{20}$$

where

freeze(%) = percentage of freeze,
w_{unfrozen} = gravimetric water content of specimen at completely unfrozen status,
w_t = gravimetric water content at time t of freezing–thawing specimen, and
w_{frozen} = gravimetric water content in completely frozen specimen.

Substituting Equation 19 into Equation 20 and simplifying the terms, the degree of freeze–thaw can be estimated from TDR measured dielectric constant via the following relationship:

$$\begin{aligned}\text{freeze}(\%) &= \frac{w_{\text{unfrozen}} - w_t}{w_{\text{unfrozen}} - w_{\text{frozen}}} \times 100\% \\ &= \frac{\sqrt{K_{a,\text{unfrozen}}} - \sqrt{K_{a,t}}}{\sqrt{K_{a,\text{unfrozen}}} - \sqrt{K_{a,\text{frozen}}}} \times 100\%\end{aligned} \tag{21}$$

where

freeze(%) = percentage of freeze,
$K_{a,\text{unfrozen}}$ = dielectric constant of specimen completely unfrozen status,

$K_{a,t}$ = dielectric constant at time t of the freezing–thawing specimen, and
$K_{a,\text{frozen}}$ = dielectric constant in completely frozen specimen.

Equation 21 shows, for a given granular material (such as soil or concrete), that a linear relationship exists between $\sqrt{K_a}$ and degree of freeze–thaw. As the material-dependent constants in Equation 19 were automatically canceled from the numerator and denominator, the degree of freeze–thaw in Equation 21 expressed in TDR measurement does not depend on a specific type of granular matrix. This is an advantage of TDR technology for degree of determining freeze–thaw.

The degree of thaw can be defined in similar fashion. During the freeze–thaw cycle, the degree of freeze and degree of thaw is related by the following equation:

$$\text{thaw}\% = 1 - \text{freeze}\% \tag{22}$$

Applications of TDR to frozen soils were investigated by Patterson and Smith (*27*), Smith and Tice (*28*), Spaans and Baker (*29*), and Kahimba and Ranjan (*30*), and others. TDR was found to be able to measure specifically the amount of unfrozen water in soil, owing to the significant drop of the dielectric constant of free water (around 81) as it changes into ice (around 3.2) (*31, 32*). The ability of TDR to measure the unfrozen water content provides a method to directly assess the status of freeze–thaw development.

Development of New Nonintrusive Time-Domain Reflectometry Sensor

These previous investigations mostly used commercial TDR probes that are intrusive and thus not suitable for use in concrete. To overcome the shortcomings, an innovative TDR tube sensor was developed in the laboratory, where the waveguides for electromagnetic wave are installed along the inner surface of the tube (Figure 9). The TDR waveguides, which were made of copper strips of equal length, were mounted onto the inner surface of the selected polyvinyl chloride tube by special adhesive. The size of tube can be selected with internal diameter matches that are slightly larger than the diameter of the specimen. Doing this allows for nondestructively monitoring the freezing–thawing processes in concrete (Figure 9).

Experimental Evaluation

A 2-in.-diameter sample was used to evaluate the performance of this tube sensor in freezing status measurement. The material was an ordinary mortar mixture with the design of 28-day strength of 3,000 psi.

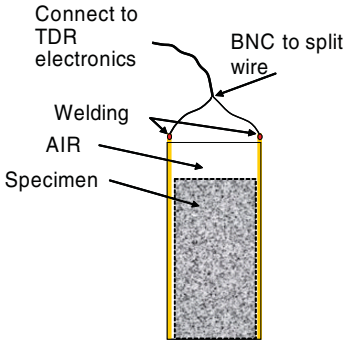

FIGURE 9 Nonintrusive TDR tube sensor.

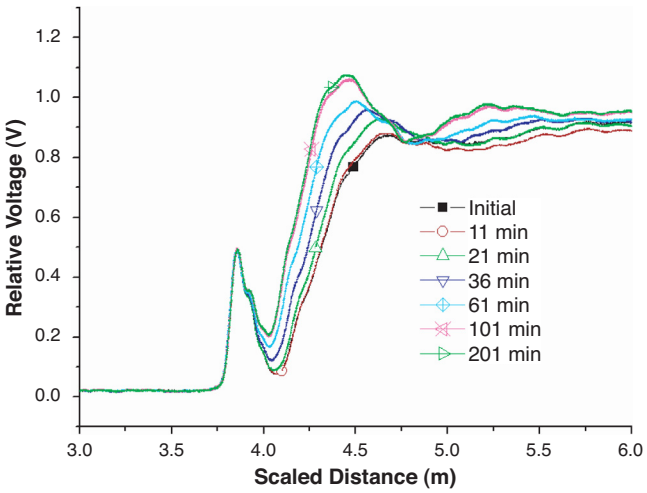

FIGURE 10 TDR signals after freezing process starts.

The TDR system used was TDR100, manufactured by Campbell Scientific Inc. The water content of this sample after 7 days of curing was measured by oven-drying and was found to be around 15%. The specimen was then placed in to a freezer that maintains a temperature –15°C and was subjected to the freezing process. Figure 10 shows the monitored TDR signals during the freezing process (being subjected to a freezer), with use of the new TDR tube sensor. From this figure, a noticeable trend of change can be observed as freezing proceeds. The TDR signals are responsive to the freezing evolution. When freezing processes are accomplished, the TDR signals become stable. Signals in Figure 10 indicate that the specimen become completely frozen in about 100 min.

Signals in Figure 10 can be analyzed using the common TDR signal analyses procedures (*23*). Figure 11 shows the degree of freezing determined from the measured TDR signals at different freezing times, using Equation 21. The degree of freezing, together with the initial water content, give estimation of the internal crystalline pressure during freezing. This will provide an important input variable for the simulation model described in the previous section.

CONCLUSIONS

Internal frost damage is a major factor affecting the durability of concrete in cold regions. This paper investigates the basic mechanism of internal frost damage in concrete. Crystallization pressure resulting from ice nucleation inside of the capillary pores can cause the crack initiation and propagation when this pressure exceeds the

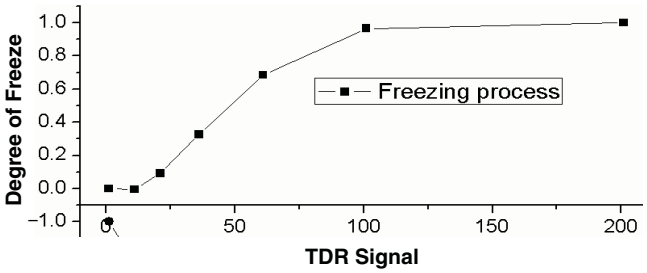

FIGURE 11 Degree of freezing determined from TDR signal analyses.

concrete tensile strength. Under a subcooling temperature, the crystallization pressure of a cylinder pore with a hemispherical end was calculated with thermodynamic analysis.

The XFEM fracture simulation was conducted on a homogeneous beam sample and an imaging beam sample under crystallization pressure. A straight crack line was predicted for the homogeneous sample. The imaging sample was generated with imaging process and ellipse fitting techniques to capture the aggregate microstructure of the actual laboratory-tested specimen. The crack propagation under the symmetric crystallization pressure loading was compared with middle-notched beam bending test because of open-mode fracture in both loading cases. The crack path of the imaging sample matches well with the fracture pattern of the tested specimen. Results indicated that the XFEM has abilities in predicting frost-induced crack behavior within heterogeneous concrete.

In parallel with the numerical simulation model, an innovative TDR tube sensor was developed to nondestructively monitor the freezing process. Experiments were conducted to evaluate the performance of this sensor. Results indicated that the new sensor signals are responsive to the freezing process. With further refinements, this sensor would provide a useful tool to investigate the influence of freezing on the mechanical properties of concrete as well as the frost damage mechanism. The sensor data will provide important information on the amount of formed ice from the saturated water within the pore system for calculating the crystallization pressure generated from pores. With this calculated pressure, the developed micromechanics model can simultaneously predict the crack propagation under the freezing process. In the ongoing study, the performance of micromechanics models and sensor technologies will be validated with a cause and sequence freezing test program by using TDR status monitoring and acoustic emission damage detection. Furthermore, the integrative computational model and innovative sensor will be developed into practical tools to guide the design of concrete that is resistant to freezing damage.

ACKNOWLEDGMENT

The partial support of this research by the National Science Foundation is gratefully appreciated.

REFERENCES

1. Sullivan, E. J. *Long-Term Cement Consumption Outlook.* Portland Cement Association, Skokie, Ill., 2006.
2. Portland Cement Association. Frequently Asked Questions: What Causes Concrete Crack? http://www.cement.org/tech/faq_cracking.asp. Accessed August 8, 2011.
3. Concrete Experts International. Freeze–Thaw Deterioration of Concrete. http://www.concrete-experts.com/pages/ft.htm. Accessed August 8, 2011.
4. Mehta, P. K., and P. J. M. Monteiro. *Concrete: Microstructure, Properties, and Materials,* 3rd ed. McGraw-Hill Companies, Inc., New York, 2006.
5. Litvan, G. G. Phase Transitions of Adsorbates: VI, Effect of Deicing Agents on the Freezing of Cement Paste. *Journal of the American Ceramic Society,* Vol. 58, No. 1–2, 1975, pp. 26–30.
6. Kaufmann, J. Experimental Identification of Damage Mechanisms in Cementitious Porous Materials on Phase Transition of Pore Solution Under Frost Deicing Salt Attack. *EMPA* (Swiss Federal Laboratories for Materials Testing and Research), 248, pp. 7–177.
7. Powers, T. C., and R. A. Helmuth. Theory of Volume Changes in Hardened Portland-Cement Paste During Freezing. In *Highway Research Board Proceedings,* Vol. 32, 1953, pp. 285–297.
8. Valenza, J. J. II, and G. W. Scherer. Mechanism for Salt Scaling. *Journal of the American Ceramic Society,* Vol. 89, No. 4, 2006, pp. 1161–1179.
9. Valenza, J. J. II, and G. W. Scherer. Mechanisms of Salt Scaling. *Materials and Structures/Materiaux et Construction*s, Vol. 38, No. 278, 2005, pp. 479–488.
10. Valenza J. J. II, and G. W. Scherer. A Review of Salt Scaling: II. Mechanisms. *Cement and Concrete Research,* Vol. 37, No. 7, 2007, pp. 1022–1034.
11. Scherer, G. W., and J. J. Valenza II. Mechanisms of Frost Damage. In *Materials Science of Concrete,* Vol. VII (F. Young and J. Skalny, eds.), John Wiley & Sons, New York, 2005, pp. 209–246.
12. Scherer, G. W. Crystallization in Pores. *Cement and Concrete Research,* Vol. 29, No. 8, 1999, pp. 1347–1358.
13. Everett, D. H. The Thermodynamics of Frost Damage to Porous Solids. *Transactions of the Faraday Society,* Vol. 57, 1961, pp. 1541–1551.
14. Defay, R., and I. Prigogine. *Surface Tension and Absorption.* John Wiley & Sons, New York, 1966.
15. Moës, N., J. Dolbow, and T. Belytschko. A Finite Element Method for Crack Growth Without Remeshing. *International Journal for Numerical Methods in Engineering,* Vol. 46, No. 1, 1999, pp. 131–150.
16. Marc, D. A Study of the Representation of Cracks with Level Sets. *International Journal for Numerical Methods in Engineering,* Vol. 70, No. 11, 2007, pp. 1261–1302.
17. Pais, M. J., and N. H. Kim. Modeling Failure in Composite Materials with the Extended Finite Element and Level Set Methods. *Proc., 50th AIAA/ASME/ASCE/AHS/ASC Structures, Structural Dynamics, and Materials Conference* (AIAA 2009-2393), Palm Springs, Calif., Curran Associates, Inc., Redhook, NY, 2009.
18. Moës, N., M. Cloirec, P. Cartraud, and J. F. Remacle. A Computational Approach to Handle Complex Microstructure Geometries. *Computer Methods in Applied Mechanics and Engineering,* Vol. 192, No. 28–30, 2003, pp. 3163–3177.
19. Jeon, I., K.-J. Kang, and S. Im. Stress Intensities at the Triple Junction of a Multilevel Thin Film Package. *Microelectronics Reliability,* Vol. 48, No. 5, 2008, pp. 749–756.
20. Stolarska, M., D. L. Chopp, N. Moës, and T. Belytschko. Modelling Crack Growth by Level Sets in the Extended Finite Element Method. *International Journal for Numerical Methods in Engineering,* Vol. 51, No. 8, 2001, pp. 943–960.
21. Wang, J., Y. W. Tang, and X. C. Zeng. Solid-Liquid Interfacial Free Energy of Water: A Molecular Dynamics Simulation Study. *Journal of Chemical Theory and Computation,* Vol. 3, No. 4, 2007, pp. 1494–1498.
22. Ng, K., and Q. Dai. An Extended Finite Element Model for Predicting Micro-Crack Evolution and Fracture Properties Within Idealized Cement-Based Materials. *Journal of Engineering Mechanics,* forthcoming.
23. Dowding, C. H., ed. *Proc., 2nd International Symposium and Workshop on Time Domain Reflectometry for Innovative Geotechnical Applications,* Northwestern University, Evanston, Ill., 2001.
24. O'Connor, K. M., C. H. Dowding, and C. C. Jones. *Time Domain Reflectometry in Environmental, Infrastructure, and Mining Applications.* Special Publication SP 19-94. Bureau of Mines, U.S. Department of the Interior, 1994.
25. Topp, G. C., J. L. Davis, and A. P. Annan. Electromagnetic Determination of Soil Water Content: Measurements in Coaxial Transmission Lines. *Water Resources Research,* Vol. 16, No. 1, 1980, pp. 574–588.
26. Siddiqui, S. I., and V. P. Drnevich. *Use of Time Domain Reflectometry for the Determination of Water Content and Density of Soil.* FHWA/IN/JHRP-95/9. Purdue University, West Lafayette, Ind., 1995.
27. Patterson, D. E., and M. W. Smith. The Measurement of Unfrozen Water Content by Time Domain Reflectometry: Results from Laboratory Tests. *Canadian Geotechnical Journal,* Vol. 18, No. 1, 1981, pp. 131–144.
28. Smith, M. W., and A. R. Tice. Measurement of the Unfrozen Water Content of Soils: Comparison of NMR and TDR Methods. *CRREL Report 88-18,* Cold Regions Research and Engineering Laboratory, U.S. Army Corps of Engineers, Hanover, N.H.,1988, pp. 1–11.
29. Spaans, E. J. A., and J. M. Baker. Examining the Use of Time Domain Reflectometry for Measuring Liquid Water Content in Frozen Soil. *Water Resources Research,* Vol. 31, No. 12, 1995, pp. 2917–2925.
30. Kahimba, F. C., and R. S. Ranjan. Soil Temperature Correction of Field TDR Readings Obtained Under near Freezing Conditions. *Canadian Biosystems Engineering,* Vol. 45, No. 1, 2007, pp. 19–26.
31. Evett, S. R. Soil Water Measurement by Time Domain Reflectometry. In *Encyclopedia of Water Science* (B. A. Stewart and T. A. Howell, eds.), Marcel Dekker, Inc., New York, 2003, pp. 894–898.
32. Warrick, A. W. *Soil Physics Companion.* CRC Press, Boca Raton, Fla., 2002.

The Properties of Concrete Committee peer-reviewed this paper.